Electronic Supplementary Material (ESI) for Biomaterials Science.

Supporting Information:

Reinforcing hydrogels with *in situ* formed amorphous $CaCO_3$

Huachuan Du,† Tianyu Yuan, Ran Zhao, Matteo Hirsch, Michael Kessler, Esther Amstad*

Soft Materials Laboratory, Institute of Materials, École Polytechnique Fédérale de Lausanne (EPFL), 1015 Lausanne, Switzerland

E-mail : esther.amstad@epfl.ch

†Present address: Laboratory of Macro-Organic Chemistry, Department of Chemical Engineering and Chemistry, Eindhoven University of Technology (TU/e)

1. Modified gas-diffusion mineralization method

Composition and structure of formed minerals and their interactions with polyacrylamide (PAM) hydrogels

To check the structure of the minerals formed in the PAM hydrogel in the presence of different concentrations of $CaCl_2$, we characterize all these hydrogels with X-Ray Diffraction (XRD) and Fourier Transform infrared spectroscopy (FTIR).[1,2] The minerals formed in all samples are composed of vaterite and calcite, as confirmed by their characteristic diffraction peaks shown in Figure S1. Similarly, they display the ν_3 absorption peaks around 1430 cm^{-1}, the ν_1 peaks at 1088 cm^{-1}, the ν_2 peaks at 872 cm^{-1} and the ν_4 peaks at 742 and 712 cm^{-1}, characteristic peaks for crystalline $CaCO_3$ in FTIR, as shown in Figure S2. Specifically, the ν_4 absorption peaks at 742 cm^{-1} indicate the presence of vaterite and those at 712 cm^{-1} indicate the presence of calcite, in good agreement with the XRD results.

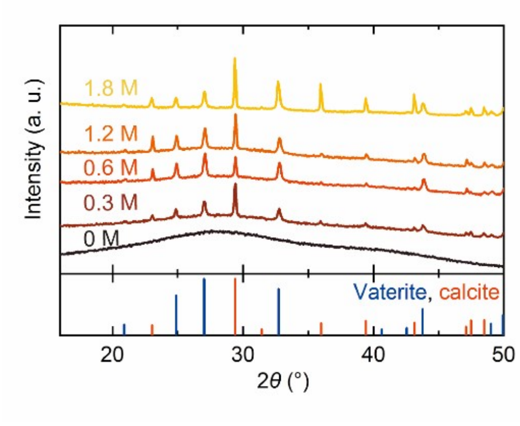

Figure S1. XRD patterns of PAM hydrogels produced from monomer solutions containing different concentrations of $CaCl_2$. The concentration of $CaCl_2$ is labelled next to the respective pattern.

To characterize the interaction between $CaCO_3$ and hydrogel matrix, we perform FTIR analysis.[3] After the mineralization with $CaCO_3$ crystals, the characteristic peak corresponding to the C=O stretching of the PAM hydrogel shifts from 1662 cm^{-1} to 1655 cm^{-1} and that at 3200-3340 cm^{-}

[1] corresponding to the N-H stretching splits into two peaks, indicating the chemical interaction between $CaCO_3$ crystals and the PAM hydrogel network.[4–7]

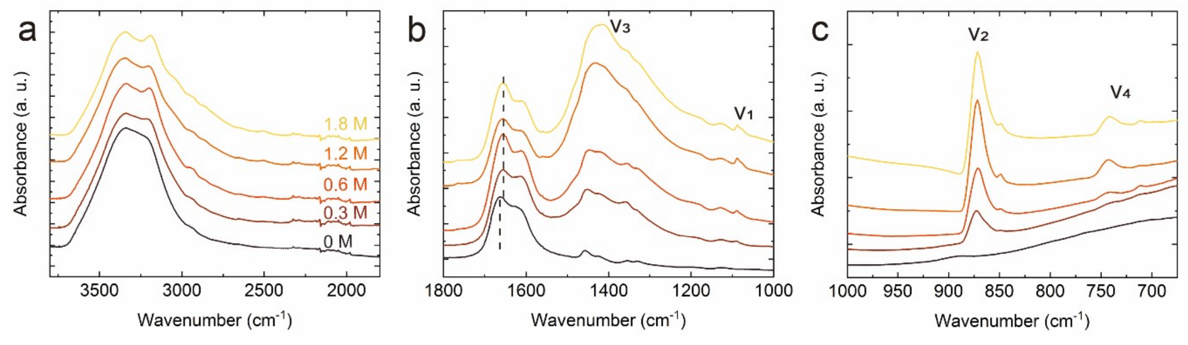

Figure S2. FTIR spectra of PAM hydrogels produced from monomer solutions containing different concentrations of $CaCl_2$.

Distribution of $CaCO_3$ crystals within the hydrogel

To test if our mineralization method avoids the uncontrolled formation of $CaCO_3$ layers on the PAM hydrogel surface, we visualize the cross-section of the mineralized PAM hydrogel using scanning electron microscopy (SEM). We do not observe any sign of mineral surface layers, as shown in Figure S3. Instead, the formed $CaCO_3$ crystals are uniformly distributed throughout the cross-section of the sample. We assign the homogeneous mineralization to the slow decomposition of ammonium carbonate that ensures a homogeneous distribution of carbonate ions throughout the hydrogel. Before $(NH_4)_2CO_3$ can initiate the mineralization, the following reactions must take place:[8]

$$NH_3 + H_2O \rightleftharpoons NH_3 \cdot H_2O$$

$$NH_3 \cdot H_2O \rightleftharpoons NH_4^+ + OH^-$$

$$CO_2 + H_2O \rightleftharpoons H_2CO_3$$

$$H_2CO_3 \rightleftharpoons H^+ + HCO_3^-$$

$$HCO_3^- \rightleftharpoons H^+ + CO_3^{2-}$$

$$H^+ + OH^- \rightleftharpoons H_2O$$

$$Ca^{2+} + CO_3^{2-} \rightleftharpoons CaCO_3$$

The fact that we observe a homogeneous mineralization throughout the hydrogel suggests that the formation of carbonate ions is slower than the diffusion of CO_2 and NH_3 gas molecules within the hydrogel. As a result, when carbonate ions become available to initiate the mineralization, they are homogeneously distributed within the hydrogel. Note that this is likely only true for thin hydrogels like the ones reported in this work that have a thickness of 2 mm.

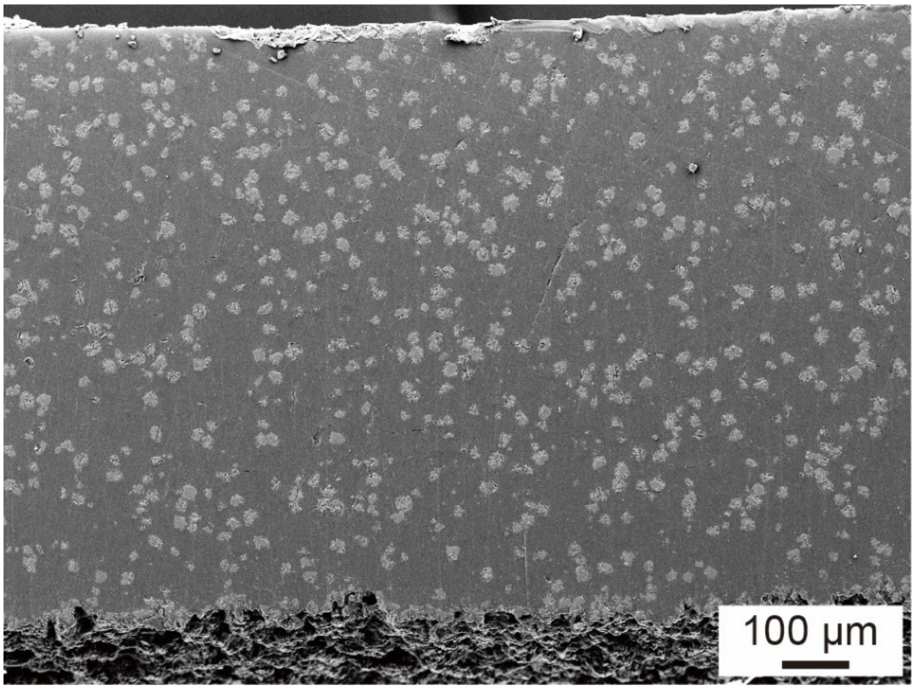

Figure S3. SEM image of the polished cross-section of a mineralized PAM hydrogel produced from a monomer solution containing 0.6 M $CaCl_2$. To better visualize the distribution of $CaCO_3$ crystals, the PAM hydrogel network is processed to collapse it into a dense matrix.

Quantification of $CaCO_3$ mineral content

To quantify the mineral content in the hydrogels, we characterize them using thermogravimetric analysis (TGA). Hydrogels are washed thoroughly with water to avoid any influence of soluble salts contained in the hydrogels. They are subsequently dried at 60 ℃ in the oven overnight. TGA measurements are performed under a constant flow of nitrogen gas and the results are illustrated in Figure S4a. We estimate the weight of the pure hydrogel by evaluating the weight loss in the temperature range between 200 °C to 680 °C, where PAM decomposes into carbon black. As PAM hydrogels decompose into solid carbon black, we take into account the weight of the remaining carbon black above 680 °C by calculating the mass of the hydrogel. Assuming the ratio between the weight loss corresponding to the decomposition of PAM and the weight of the remaining carbon black remains the same for all mineralized hydrogels, we obtain the weight of the hydrogel in each mineralized sample. We calculate the weight of $CaCO_3$ minerals from the weight loss in the temperature range between 680 °C to 850 °C, where $CaCO_3$ decomposes into solid CaO and CO_2 gas.[1] By combining these results, we obtain the weight fraction of $CaCO_3$ crystals ($W_{\mathrm{dry,CaCO3}}$) for different dry hydrogels, as summarized in Figure S4c.

To test if the assumption for the carbon black causes a bias for estimating the mineral content, we perform TGA measurements on several samples under a constant flow of air, as shown in Figure S4b. In this case, the PAM hydrogel is fully decomposed into volatile gases. However, the temperature range corresponding to the decomposition and combustion of the PAM hydrogel overlaps with that corresponding to the decompositon of $CaCO_3$. Yet, as the remaining solid phase at 850 °C is expected to be only CaO, its weight can be used to calculate the weight of $CaCO_3$ contained in each sample. The rest of the weight of each sample is expected to be that of the PAM hydrogel. Similarly, we obtain the $W_{\mathrm{dry,CaCO3}}$ in the mineralized hydrogels measured under air flow, as exemplified in Figure S4c. The results of the $CaCO_3$ mineral content obtained from these two types of TGA measurements agree well with the theoretical values calculated by assuming a complete conversion of $CaCl_2$ into $CaCO_3$. These results prove the reliability of our methods to quantify the $CaCO_3$ content in mineralized hydrogels.

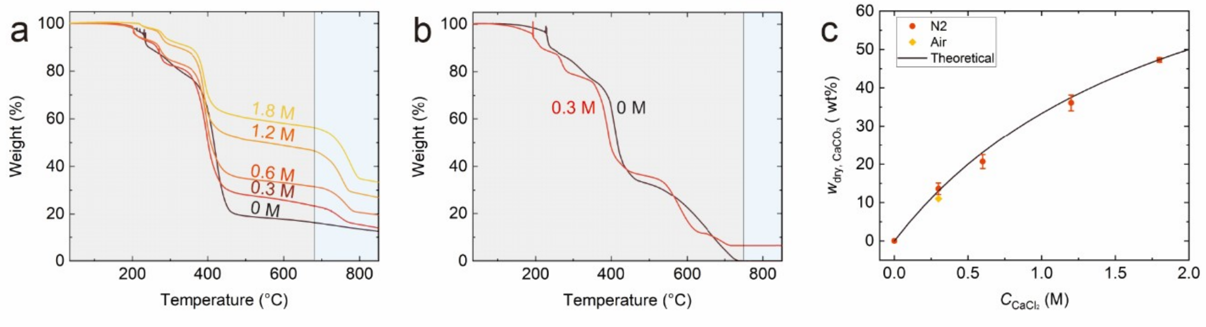

Figure S4. (a-b) TGA curves of dry PAM hydrogels produced from monomer solutions containing different concentrations of $CaCl_2$ measured under (a) an N_2 gas atmosphere and (b) in air. (c) Weight fraction of $CaCO_3$ crystals ($W_{dry,CaCO3}$) in dry hydrogels as function of the concentration of $CaCl_2$. The values measured from TGA are indicated with dots and the theoretical values calculated by assuming a complete conversion of $CaCl_2$ into $CaCO_3$ are indicated with the black line.

Water content of neat and mineralized PAM hydrogels

To minimize the dehydration of hydrogels during the mineralization process, a humid environment is created in the well-sealed petri dish. To quantify the water contents of PAM hydrogels, we measure their initial weights (m_0) and their weights after annealing them at 100 °C for 1 week (m_1). The water fractions in these samples can be calculated with $(m_0 - m_1)/ m_0$. The measured water contents of different hydrogel samples are similar to those present in the initial solution, as summarized in Table S1. These results suggest that the dehydration or swelling of hydrogels during the mineralization is negligible.

Table 1. Theoretically expected and measured water contents of different hydrogel samples.

Hydrogel samples	**Theoretical water content (wt%)**	**Measured water content (wt%)**
Non-mineralized PAM	80	77.4 ± 0.8
Mineralized PAM (1.8 M $CaCl_2$)	53.2	52.5 ± 0.2
Mineralized PAM (0.3 M $CaCl_2$, 1.5 M $CaCl_2$)	51.1	52.0 ± 0.5

2. Influence of $CaCO_3$ crystal content

Mechanical properties of PAM hydrogels mineralized with $CaCO_3$ crystals

To quantify the mechanical properties of hydrogels, we perform tensile tests on unnotched and notched rectangular hydrogels. The stress-strain curves of the unnotched samples are used for the calculation of the Young's moduli of hydrogels, as shown in Figure S5a. The initial linear regime ranging from 5% to 25% strain of unnotched hydrogels are fitted to calculate the Young's moduli, as summarized in Figure S6. To estimate the fracture energy of hydrogels, we use the notched samples to determine the critical extension for the crack initiation (ΔL_c), as illustrated in the force (F)-extension (ΔL) curves in Figure S5b. This value is subsequently used to calculate the fracture energy (Γ) of the corresponding unnotched samples as follows,[9,10]

$$\Gamma = \int_0^{\Delta L_c} F \, d\Delta L \Big/ A$$

Where A is the area of cross-section of hydrogels. The calculation of $\int_0^{\Delta L_c} F \, d\Delta L$ is indicated with the grey-filled area in Figure S5b. To ensure the reproducibility of the results obtained with this method, at least three repetitions are performed on unnotched and notched samples, as demonstrated in Figure S5c.

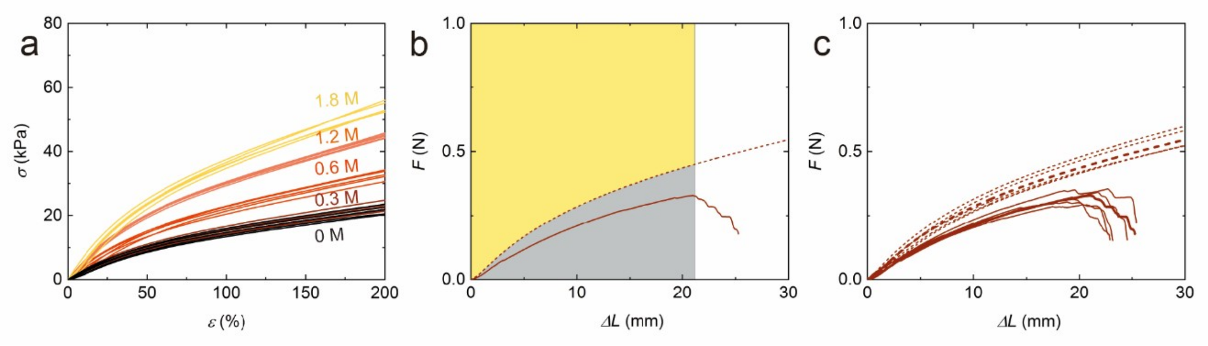

Figure S5. (a) Stress-strain curves measured on PAM hydrogels produced from monomer solutions containing different concentrations of $CaCl_2$. (b) Schematic illustration of the calcuation of the fracture energy of hydrogels based on the force (F)-extension ($\mathit{\Delta}L$) curves obtained from the notched and unnotched samples. The curve for the notched sample is shown as a solid line, that for the unnotched one as a dashed line. (c) All the force (F)-extension ($\mathit{\Delta}L$) curves are measured for the mineralized hydrogels produced from a monomer solution containing 0.3 M $CaCl_2$. The respresentative curves shown in the main paper are highlighted with thicker lines.

The Guth-Gold model describes the dependence of Young's moduli of composite hydrogels on the volume fraction of non-interacting filler particles.[11,12]

$$E = E_0\,(1 + 2.5\Phi + 14.1\Phi^2)$$

Where E_0 is the Young's modulus of neat hydrogels and $\mathit{\Phi}$ the volume fraction of inorganic fillers. To determine if there is an interaction between $CaCO_3$ crystals and the PAM hydrogel, we compare our measured Young's moduli with those predicted from the Guth-Gold model. We estimate the volume fraction of $CaCO_3$ crystals ($\mathit{\Phi}_{\mathrm{CaCO3}}$) in as-prepared hydrogels based on the previous results of the weight fraction of $CaCO_3$ crystals ($W_{\mathrm{dry,CaCO3}}$) in the dry hydrogels as well as the initial weights of water and acrylamide contained in the solution. By assuming the density of water to be 1 g cm^{-3}, that of PAM to be 1.2 g cm^{-3}, and that of $CaCO_3$ to be 2.71 g cm^{-3}, we obtain the approximate values of $\mathit{\Phi}_{\mathrm{CaCO3}}$. Hence, we can plot the Young's moduli of our hydrogel samples as a function of $\mathit{\Phi}_{\mathrm{CaCO3}}$ and the prediction from the Guth-Gold model, as illustrated in Figure 6c.

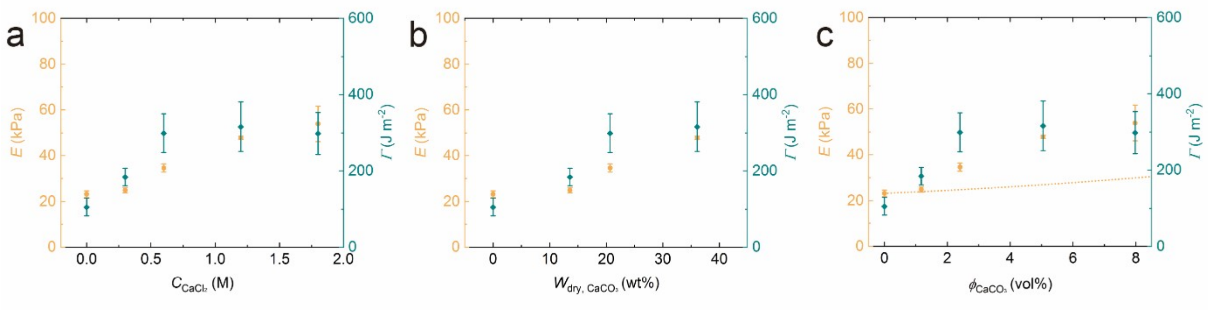

Figure S6. Young's moduli (E) and fracture energy (Γ) of hydrogels as function of (a) the initial concentration of $CaCl_2$ (C_{CaCl2}) contained in monomer solutions, (b) weight fraction of $CaCO_3$ crystals ($W_{dry,CaCO3}$) in dry hydrogels and (c) the volume fraction of $CaCO_3$ crystals (Φ_{CaCO3}) in as-prepared hydrogels.

Morphology of neat and mineralized hydrogels

We use scanning electron microscopy (SEM) to visualize the morphology of neat and mineralized PAM hydrogels. To better maintain the morphology of the neat PAM hydrogel network during the sample preparation, we dry the hydrogel using a freeze dryer. The size of the pores possessed by PAM hydrogels is polydisperse with a diameter ranging from 100 nm to 2 µm, as shown in Figure S7a to S7c. To avoid artifacts from soluble salts contained in the hydrogels in the visualization of the $CaCO_3$ morphology, we use a solvent to remove them before drying the sample. To minimize the effect of solvent on the swelling of the hydrogel networks and to ensure a good solubility of salts within it, we choose methanol to wash our hydrogels thoroughly prior to their drying at room temperature overnight. The morphology of the resulting hydrogels is exemplified on a hydrogel produced from a monomer solution containing 1.8 M $CaCO_3$, as shown in Figure S7d to S7f.

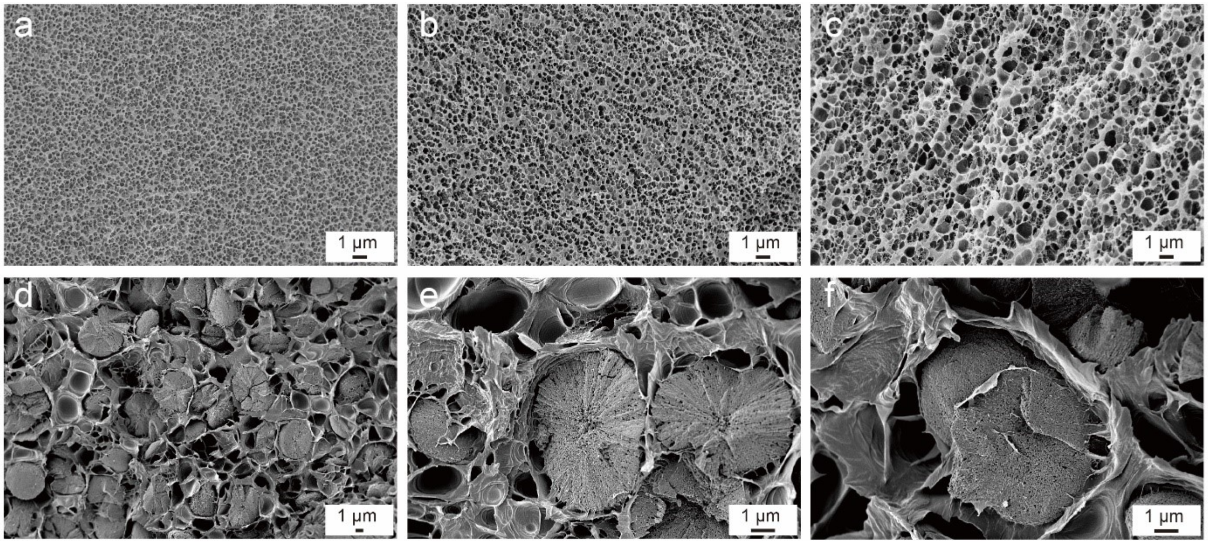

Figure S7. SEM images of (a-c) the neat PAM hydrogel and (d-f) the hydrogel mineralized from a monomer solution containing 1.8 M $CaCl_2$.

3. Influence of Mg^{2+} additive

Structure of formed $CaCO_3$ minerals and their interactions with PAM hydrogels

The structure of the minerals formed in the presence of Mg^{2+} is characterized using FTIR. The position of the ν_2 and ν_4 absorption peaks often provides an easy means to distinguish between the amorphous $CaCO_3$ (ACC) and different crystalline polymorphs of $CaCO_3$. If the Mg/Ca molar ratios are 1/1 and 2/1, the formed $CaCO_3$ minerals are calcite, as confirmed by their characteristic ν_2 peak at 871 cm^{-1} and ν_4 peak at 711 cm^{-1} shown in Figure S8c. If Mg/Ca molar ratios are 3/1 and 4/1, certain regions of these samples have similar features as those observed for calcite. However, other regions of these samples display the ν_2 peak at 860 cm^{-1} and a broad ν_4 absorption band that are characteristic for ACC. Hence, both calcite and ACC form in these hydrogels. If the Mg/Ca molar ratio is further increased to 5/1, all samples display the characteristic absorption peaks of ACC.

Similar to the PAM hydrogels mineralized in absence of Mg^{2+}, the characteristic peaks corresponding to the C=O stretching of PAM shift from 1662 cm^{-1} to 1656 cm^{-1} and those at 3200-

3340 cm^{-1} corresponding to the N-H stretching of PAM split into two peaks, indicating the chemical interaction between the PAM hydrogel and formed minerals.[4–7]

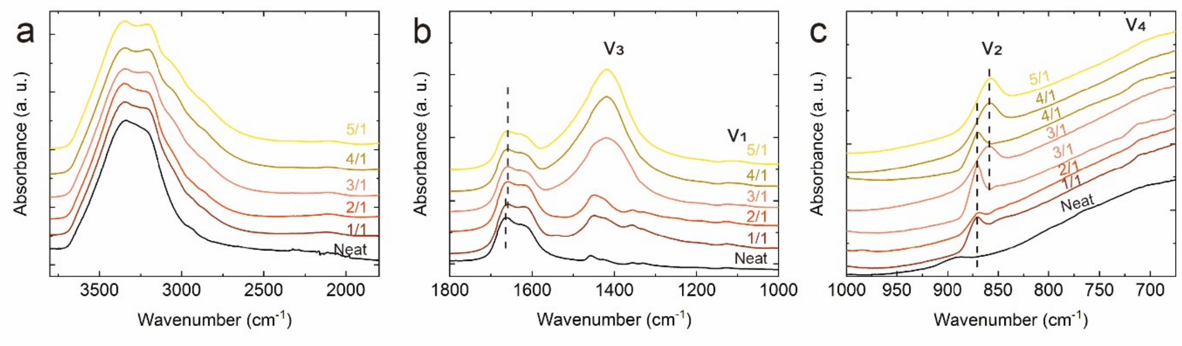

Figure S8. FTIR spectra of PAM hydrogels produced from monomer solutions containing 0.3 M $CaCl_2$ and different concentrations of $MgCl_2$. The molar ratio between Mg^{2+} and Ca^{2+}, Mg/Ca, is indicated next to the respective spectrum.

Morphology of mineralized hydrogels

Within PAM hydrogels mineralized with different Mg/Ca ratios, the size of formed mineral particles, their location, and their connections with the hydrogel network are visualized using SEM, as exemplified in Figure S9 and S10.

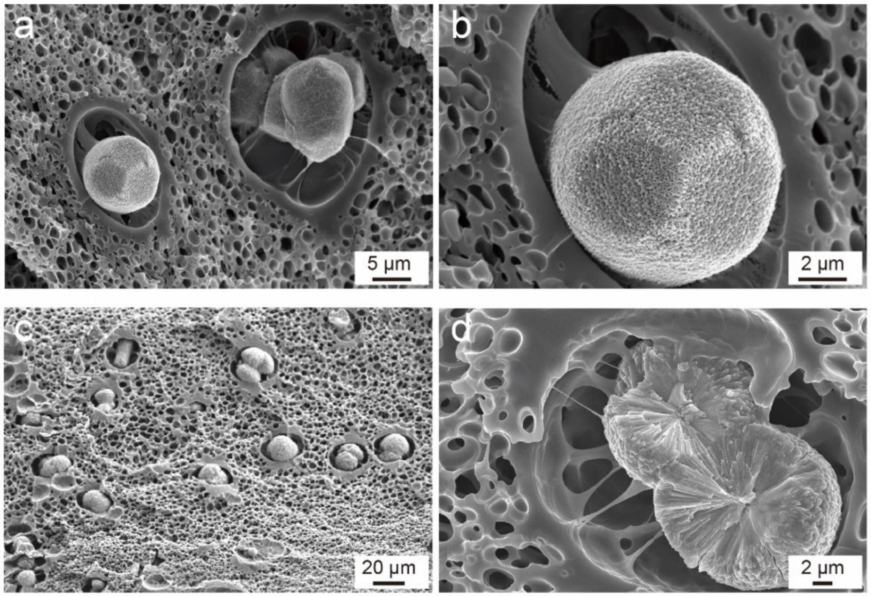

Figure S9. SEM images of mineralized PAM hydrogels produced with a Mg/Ca ratio of (a,b) 1/1 and (c,d) 2/1.

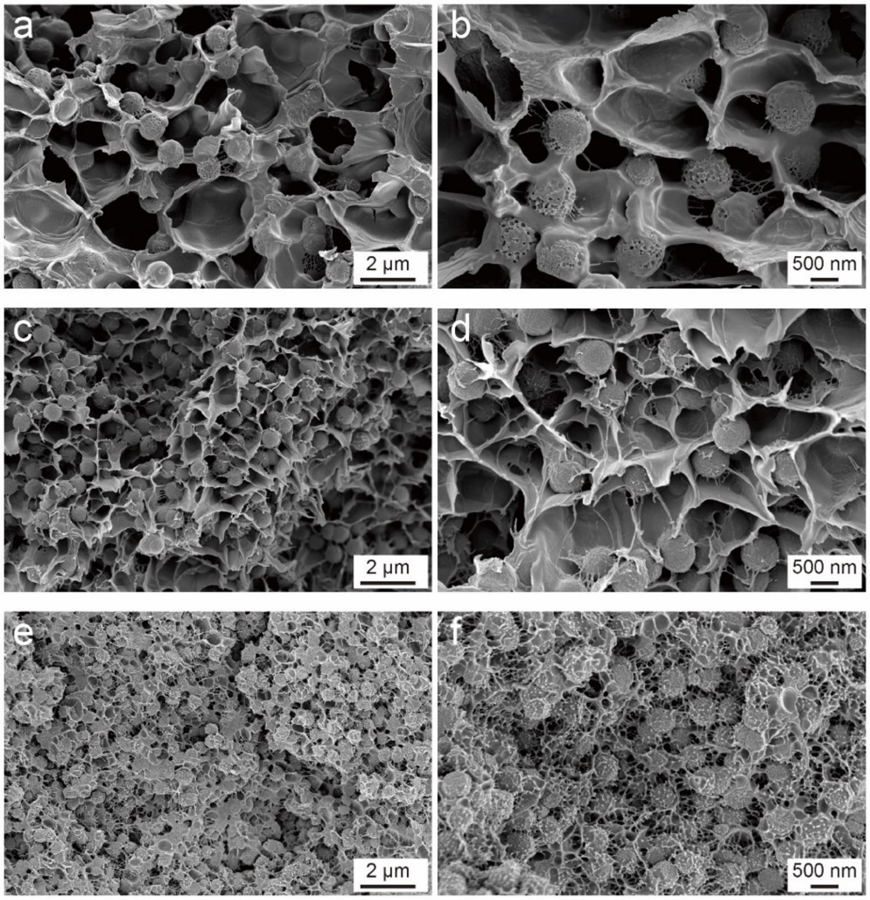

Figure S10. SEM images of mineralized PAM hydrogels produced with a Mg/Ca ratio of (a,b) 3/1, (c,d) 4/1 and (e,f) 5/1.

Mechanical properties

To quantify the mechanical properties of hydrogels mineralized in the presence of Mg^{2+}, we apply a similar method as described in the Section 1. As an example, the force (*F*)-extension (*ΔL*) curves measured on samples produced with a Mg/Ca ratio of 5/1 are illustrated in Figure S11.

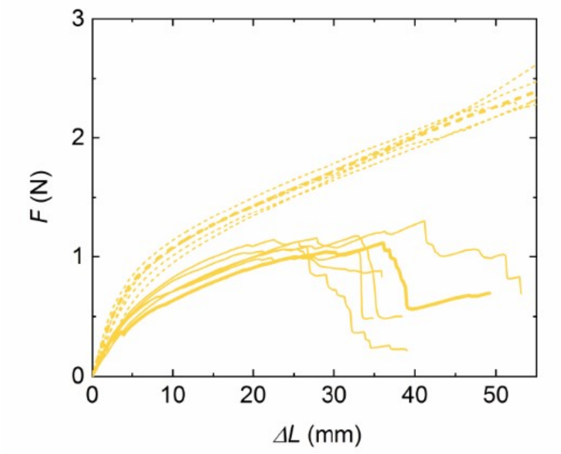

Figure S11. Force (*F*)-extension (*ΔL*) curves measured for the mineralized hydrogels produced with a Mg/Ca ratio of 5/1. The respresentative curves shown in the main paper are highlighted with thicker lines.

Influence of magnesium carbonate

To ensure that the reinforcing effect observed with high quantities of Mg^{2+} ions is not a result of the formation of more magnesium carbonate, we deliberately form magnesium carbonate inside our hydrogels. We mineralize PAM hydrogels in a solution containing 1.8 $MgCl_2$ in the absence of any $CaCl_2$. The resulting hydrogels contain many macroscopic magnesium carbonate crystals as large as a few millimeters, in contrast with the micro-sized mineral crystals or nano-sized amorphous phases obtained in calcium carbonate-containing counterparts, as exemplified in Figure S12a. Interestingly, these samples are stiffer than hydrogels mineralized with 1.8 M $CaCl_2$, but their fracture energy is lower, as summarized in Figure S12b.

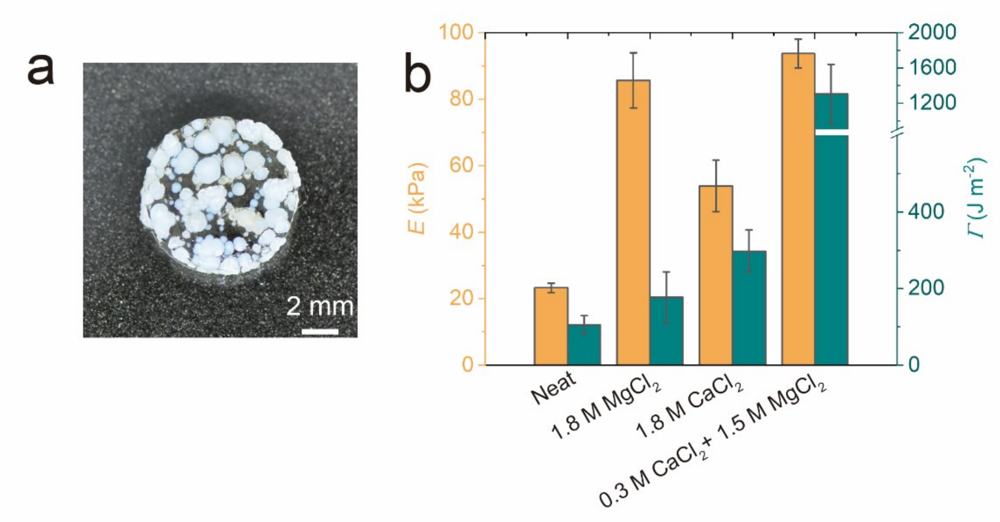

Figure S12. (a) Photograph of the PAM hydrogel mineralized in an aqueous solution containing 1.8 MgCl$_2$. (b) Comparison of Young's moduli (E) and fracture energy (Γ) of neat PAM hydrogels and those mineralized in aqueous solutions containing 1.8 M MgCl$_2$, 1.8 M CaCl$_2$ and 0.3 M CaCl$_2$ + 1.5 M MgCl$_2$.

4. Influence of the functionalization with acrylic acid (AA)

Structure of formed CaCO$_3$ minerals and their interactions with PAM-co-PAA hydrogels

Functionalization of PAM with 15 wt% AA does not significantly change the structure of the formed CaCO$_3$ particles, as indicated with XRD and FTIR spectra shown in Figure S13 and S14. Thus, if the mineralized PAM-co-PAA hydrogels are produced from a monomer solution containing 1.8 M CaCl$_2$, the formed minerals are composed of vaterite and calcite. Instead, if the mineralized PAM-co-PAA hydrogels are produced from a monomer solution containing 0.3 M CaCl$_2$ and 1.5 M MgCl$_2$, the resulting minerals are ACC. In addition, the characteristic peak corresponding to the C=O stretching of PAM shift from 1673 cm^{-1} to 1658 cm^{-1} and that at 3200-3340 cm^{-1} corresponding to the N-H stretching of PAM split into two peaks, as shown in Figure S13a and 13b, suggesting the chemical interaction between the hydrogel and the formed CaCO$_3$.[4–7]

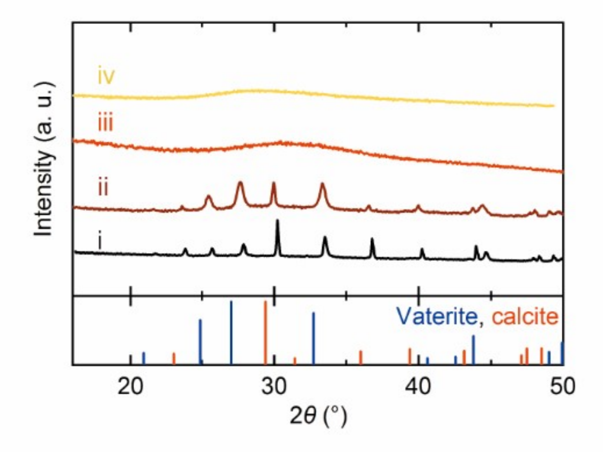

Figure S13. XRD patterns of (i, iii) PAM hydrogels produced from a monomer solution containing (i) 1.8 M $CaCl_2$ and (iii) 0.3 M $CaCl_2$ and 1.5 M $MgCl_2$ and (ii, iv) PAM-co-PAA hydrogels produced with (ii) 1.8 M $CaCl_2$ and (iv) 0.3 M $CaCl_2$ and 1.5 M $MgCl_2$.

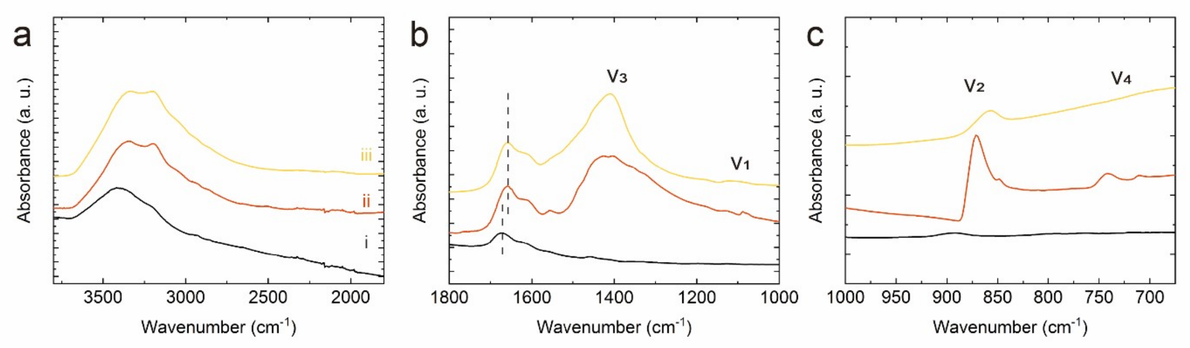

Figure S14. FTIR spectra of (i) neat PAM-co-PAA hydrogels and those produced from monomer solutions containing (ii) 1.8 M $CaCl_2$ and (iii) 0.3 M $CaCl_2$ and 1.5 M $MgCl_2$.

Morphology of mineralized hydrogels

The morphology of mineralized PAM-co-PAA hydrogels is shown in the SEM images of Figure S15 and S16.

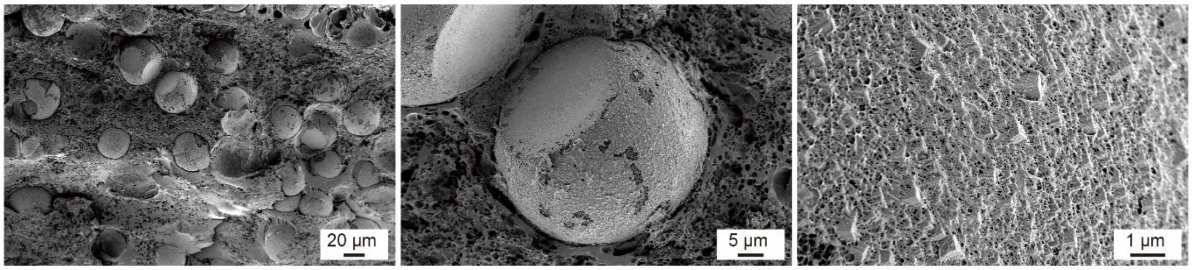

Figure S15. SEM images of mineralized PAM-co-PAA hydrogels produced from a monomer solution 1.8 M $CaCl_2$.

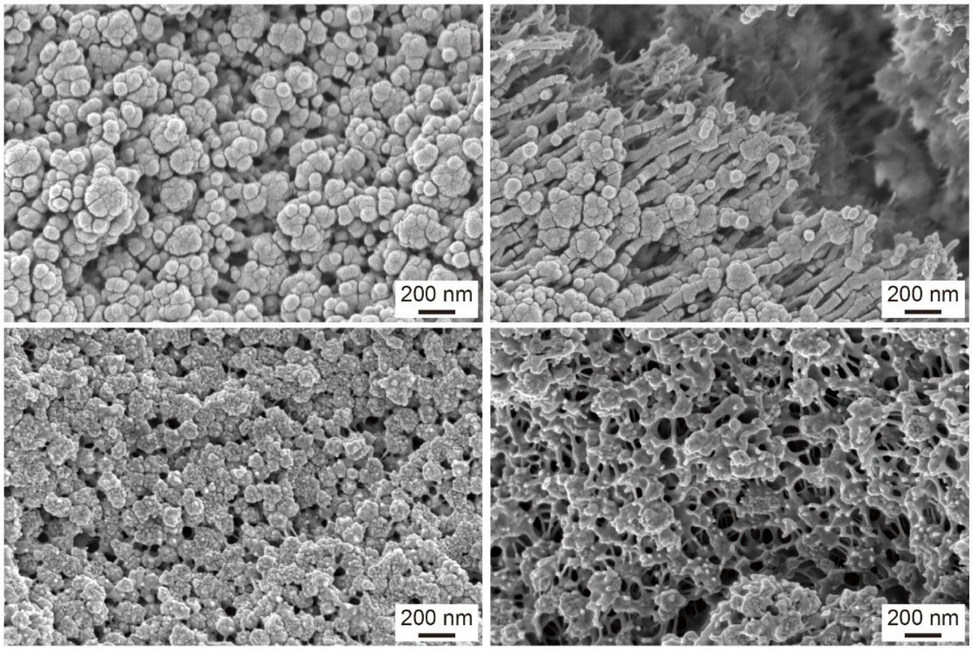

Figure S16. SEM images of mineralized PAM-co-PAA hydrogels produced from a monomer solution containing 0.3 M $MgCl_2$ and 1.5 M $CaCl_2$.

Investigation of the possible formation of an ionically crosslinked network

To test if an ionically crosslinked hydrogel network forms via the complexation between the acrylic group and the cations, including Ca^{2+} and Mg^{2+}, contained in the hydrogel, we perform mechanical tests on several control hydrogel samples. They include PAM-co-PAA hydrogels that are crosslinked from monomer solutions containing 1.8 M NaCl, 1.8 M $CaCl_2$ and 0.3 M $CaCl_2$/1.5 M $MgCl_2$. We measure these samples after they are freshly crosslinked without any exposure to ammonium carbonate that initiates the mineralization. All three types of hydrogels display similar

Young's moduli and fracture energy, as summarized in Figure S17. These results are distinctly different from those obtained in the mineralized hydrogels as shown in Figure 4e in the main paper. Because Na^+ cannot form an ionically crosslinked network with acrylic groups, the similar mechanical properties of these control samples suggest that the formation of an ionically crosslinked network by acrylic groups and Ca^{2+} or Mg^{2+} is very unlikely.

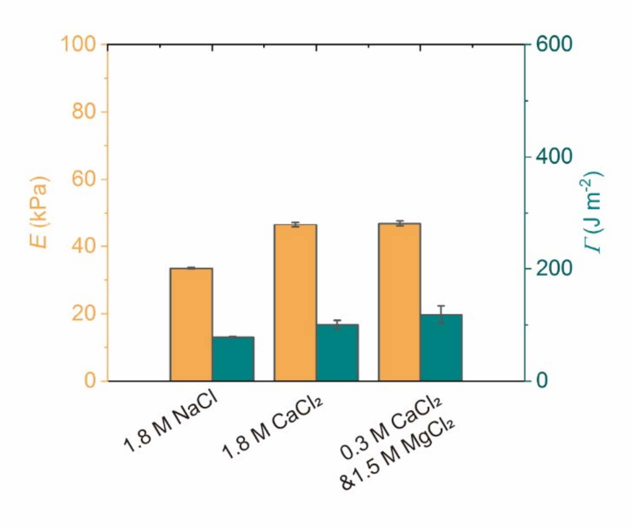

Figure S17. Young's moduli (*E*) and fracture energy (*Γ*) of freshly crosslinked PAM-co-PAA hydrogels that contain (1) 1.8 M NaCl, (2) 1.8 M $CaCl_2$ and (3) 0.3 M $CaCl_2$ and 1.5 M $MgCl_2$. No mineralization is initiated in these hydrogels.

5. References

1 H. Du, C. Courrégelongue, J. Xto, A. Böhlen, M. Steinacher, C. N. Borca, T. Huthwelker and E. Amstad, *Chem. Mater.*, 2020, **32**, 4282–4291.

2 H. Du, M. Steinacher, C. Borca, T. Huthwelker, A. Murello, F. Stellacci and E. Amstad, *J. Am. Chem. Soc.*, 2018, **140**, 14289–14299.

3 M. Guvendiren, P. A. Heiney and S. Yang, *Macromolecules*, 2009, **42**, 6606–6613.

4 Y. Yu, Z. Mu, B. Jin, Z. Liu and R. Tang, *Angew. Chem. Int. Ed.*, 2020, **59**, 2071–2075.

5 H. Jiang, G. Zhang, F. Li, Y. Zhang, Y. Lei, Y. Xia, X. Jin, X. Feng and H. Li, *Nanoscale*, 2017, **9**, 15470–15476.

6 A. S. G. Magalhães, M. P. Almeida Neto, M. N. Bezerra, N. M. P. S. Ricardo and J. P. A. Feitosa, *Quím. Nova*, 2012, **35**, 1464–1467.

7 M. K. Pal and J. Gautam, *Polym. Compos.*, 2012, **33**, 515–523.

8 J. Ihli, P. Bots, A. Kulak, L. G. Benning and F. C. Meldrum, *Adv. Funct. Mater.*, 2013, **23**, 1965–1973.

9 J.-Y. Sun, X. Zhao, W. R. K. Illeperuma, O. Chaudhuri, K. H. Oh, D. J. Mooney, J. J. Vlassak and Z. Suo, *Nature*, 2012, **489**, 133–136.

10 L. Xu, X. Zhao, C. Xu and N. A. Kotov, *Adv. Mater.*, 2018, **30**, 1703343.

11 W.-C. Lin, A. Marcellan, D. Hourdet and C. Creton, *Soft Matter*, 2011, **7**, 6578–6582.

12 S. Kim, A. U. Regitsky, J. Song, J. Ilavsky, G. H. McKinley and N. Holten-Andersen, *Nat. Commun.*, 2021, **12**, 667.